AGU PUBLICATIONS

Geochemistry, Geophysics, Geosystems

RESEARCH ARTICLE
10.1002/2014GC005579

Slip-rate-dependent melt extraction at oceanic transform faults

Hailong Bai[1] and Laurent G. J. Montési[1]

[1]Department of Geology, University of Maryland, College Park, Maryland, USA

Key Points:
- Model explains crustal thickness variations at segmented mid-ocean ridges
- Magmatism at oceanic transform faults depends on slip rate
- Melt extraction zone width and depth are 2–4 km and 15–20 km, respectively

Correspondence to:
H. Bai,
baigo@umd.edu

Citation:
Bai, H., and L. G. J. Montési (2015), Slip-rate-dependent melt extraction at oceanic transform faults, *Geochem. Geophys. Geosyst.*, *16*, 401–419, doi:10.1002/2014GC005579.

Received 17 SEP 2014
Accepted 14 JAN 2015
Accepted article online 20 JAN 2015
Published online 6 FEB 2015

Abstract Crustal thickness differences between oceanic transform faults and associated mid-ocean ridges may be explained by melt migration and extraction processes. Slow-slipping transform faults exhibit more positive gravity anomalies than the adjacent spreading centers, indicating relative thin crust in the transform domain, whereas at intermediate-spreading and fast-spreading ridges transform faults are characterized by more negative gravity anomalies than the adjacent spreading centers, indicating thick crust in the transform domain. We present numerical models reproducing these observations and infer that melt can be extracted at fast-slipping transforms, but not at slow-slipping ones. Melt extraction is modeled as a three-step process. (1) Melt moves vertically through buoyancy-driven porous flow enhanced by subvertical dissolution channels. (2) Melt accumulates in and travels along a decompaction channel lining a low-permeability barrier at the base of the thermal boundary layer. (3) Melt is extracted to the surface when it enters a melt extraction zone. A melt extraction width of 2–4 km and a melt extraction depth of 15–20 km are needed to fit the tectonic damages associated with oceanic plate boundaries that reach into the upper mantle. Our conclusions are supported by the different degrees of magmatic activities exhibited at fast-slipping and slow-slipping transforms as reflected in geological features, geochemical signals, and seismic behaviors. We also constrain that the maximum lateral distance of crust-level dike propagation is about 50–70 km.

1. Introduction

Oceanic transform faults commonly offset mid-ocean ridges, and influence the thermal structure of spreading centers and the associated melt generation [*Parmentier and Forsyth*, 1985; *Langmuir and Bender*, 1984; *Phipps Morgan and Forsyth*, 1988; *Gregg et al*., 2009; *Roland et al*., 2010; *Hebert and Montési*, 2011]. Transform faults are generally assumed to be magma-poor, as conductive cooling from the adjacent old, cold lithosphere across the transforms may efficiently reduce mantle temperature and melt production beneath the transforms [*Fox and Gallo*, 1984; *Shen and Forsyth*, 1992]. However, evidence of volcanism has been discovered at several transform faults. Ophiolite complexes in Cyprus reveal diking activities in a transform fault setting [*Murton and Gass*, 1986]. Basaltic lavas were recovered from basins in the Blanco transform at the intermediate-spreading Juan de Fuca Ridge [*Gaetani et al*., 1995], and the Garrett and Siqueiros transforms at the fast-spreading East Pacific Rise [*Hékinian et al*., 1992; *Perfit et al*., 1996]. We explore here the conditions under which melt may be extracted at oceanic transform faults and how this is related to the crustal thickness inferred from Residual Mantle Bouguer Anomalies (RMBA).

A recent compilation of RMBA from 19 oceanic ridge-transform systems [*Gregg et al*., 2007] suggests that crustal accretion is taking place along transforms but only at fast-spreading and intermediate-spreading mid-ocean ridges. At slow-spreading mid-ocean ridges, transform faults exhibit more positive gravity anomalies than the associated spreading centers. By contrast, at intermediate-spreading and fast-spreading ridges, transform faults are characterized by more negative gravity anomalies than the adjacent spreading centers [*Gregg et al*., 2007]. Gravity anomalies reflect density variations that may result from variations in rock porosity, alteration, crustal thickness, or mantle diapirism and melting. Since the most negative anomalies are not located in the transform troughs, where porosity and alteration are expected to be the highest, the RMBA differences between transforms and ridges are interpreted as consequences of crustal thickness variations: the crust at intermediate-slipping and fast-slipping transforms is thicker than at the adjacent ridge, implying active magmatism at these transforms. By contrast, no thickening is observed at slow-slipping transforms, consistent with focused mantle upwelling at slow-spreading ridges [*Lin et al*., 1990; *Gregg et al*., 2007; *Gregg et al*., 2009].

© 2015. American Geophysical Union. All Rights Reserved.

Several mechanisms have been proposed to explain volcanic activity at transform faults, including: (1) "leaky" transform faults [*Menard and Atwater*, 1969]; (2) intratransform spreading centers (ITSCs) [*Fornari et al*., 1989; *Gregg et al*., 2009]; and (3) three-dimensional migration of melt toward the transform faults [*Karson et al*., 2002; *Hebert and Montési*, 2011]. "Leaky" magmatism is induced by transtensional forces from plate reorientation on a transform fault [*Menard and Atwater*, 1969]. It has been invoked to account for magma extrusion and intrusion in the transform troughs [e.g., *Thompson and Melson*, 1972; *Murton and Gass*, 1986; *Hékinian et al*., 1992], but it does not explain the excess crust at the Clipperton transform [*Gregg et al*., 2007], which is under transpression [*Pockalny*, 1997]. Several ITSCs have been sampled and contain young volcanic rocks [e.g., *Fornari et al*., 1989]. Related crustal accretion is likely to contribute to thickened crust in the fast-slipping transform domains [*Gregg et al*., 2009], but basaltic lavas are also recovered from transform valleys away from ITSCs [*Perfit et al*., 1996; *Tepley et al*., 2004], suggesting that ITSCs alone cannot explain all of the volcanism in transforms. Recent numerical models incorporating a temperature-dependent mantle viscosity with a viscous-plastic approximation for brittle failure generate enhanced mantle upwelling beneath areas with high strain rate, like transforms [*Behn et al*., 2007; *Roland et al*., 2010]. This enhanced upwelling induces elevated temperature and thin lithosphere, which may promote melt transport toward the transform faults.

While the mechanisms mentioned above are not mutually exclusive, we focus here on the effects of three-dimensional melt migration beneath ridge-transform systems. At mid-ocean ridges, melt is generated by decompression of the mantle that rises in response to the divergence of plates. Subsequent extraction of melt can be modeled as a three-step process [*Sparks and Parmentier*, 1991; *Montési et al*., 2011; *Gregg et al*., 2012]: (1) Melt moves vertically through buoyancy-driven porous flow enhanced by subvertical dissolution channels [e.g., *Kelemen et al*., 1997]. (2) Melt accumulates in and travels along decompaction channels associated with a permeability barrier at the base of thermal boundary layer [*Sparks and Parmentier*, 1991; *Spiegelman*, 1993; *Hebert and Montési*, 2010] generally sloping toward the ridge axes. (3) Melt is extracted to the surface when it enters a melt extraction zone [*Ghods and Arkani-Hamed*, 2000]. The melt extraction zone probably reflects structural damage related to the tectonic activities at the plate boundary [*Montési et al*., 2011]. It may be present at both ridge and transform segments of oceanic spreading centers [*Hebert and Montési*, 2011]. However, the width and depth of melt extraction zone remain poorly constrained.

To explain the thickened crust and active magmatism at fast-slipping transforms, and the absence of magmatism at slow-slipping transforms, we hypothesize that, at fast-spreading ridges, the melt extraction zone intersects the permeability barrier beneath the transform fault and magma erupts along the transform, resulting in thickened crust in the transform domain; at slow-spreading ridges, the permeability barrier is too deep to intersect the melt extraction zone beneath the transform domain, resulting in little magmatic activity and thin crust along the transform fault. This hypothesis is evaluated using numerical models of the three-dimensional mantle flow and thermal structure of segmented ridges and the associated pattern of melt migration, focusing, and crustal accretion.

2. Model Setup

The oceanic crustal thickness is regarded as a direct indicator of melt delivery along mid-ocean ridges and transform faults. We predict crustal thickness variations at ridge-transform-ridge systems using three-dimensional numerical models of melt migration, and provide new constrains on the melt extraction processes at segmented mid-ocean ridges.

Mantle flow and the thermal structure beneath each ridge-transform system are solved using the commercial finite element software COMSOL Multiphysics® 4.3, which has been benchmarked for nonlinear temperature-dependent flow in geological systems [*van Keken et al*., 2008]. For a transform with length L, the computation domain is $3\times L$ long, $2\times L$ wide, and 100 km deep, with orthogonal segments of length L representing the simplified geometry of the ridge-transform-ridge system (Figure 1). Half-spreading rates are imposed on the two plates on top of the domain. Temperature on top is assumed to be 0°C, and a mantle temperature of 1375°C is imposed on the bottom. The bottom and side boundaries are set to be stress-free and open to mantle upwelling and convective flux.

A triangular mesh is defined on the top surface of the model. The element size is variable, with a maximum size of 10.5 km, and refined at the plate boundaries where the minimum element size is less than 6 km. The mesh is extruded vertically with layer spacing varying from 2.5 km near the surface to ~6 km at the bottom.

© 2015. American Geophysical Union. All Rights Reserved.

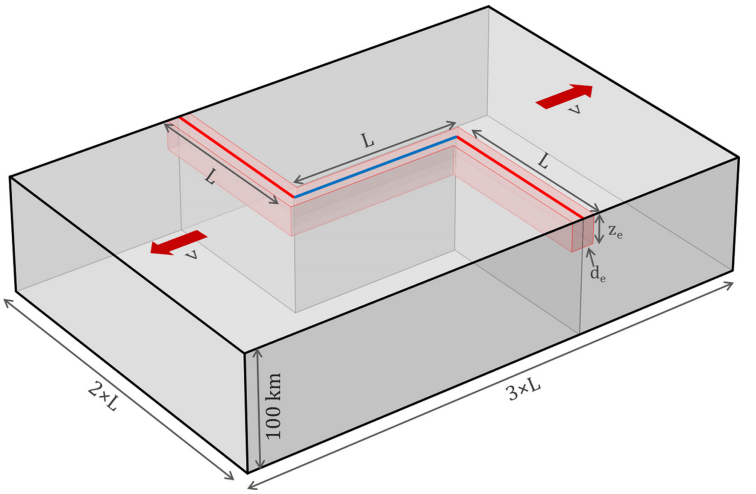

Figure 1. Model geometry of a generic ridge-transform-ridge system. The orthogonal segments on top represent ridge axes (red), and the transform fault (blue). The length of each segment is L. The computation domain is $3\times L$ long, $2\times L$ wide, and 100 km deep. Half-spreading rates are imposed on top of the two plates separated by the segments (dark red arrows). The red box denotes the melt extraction zone around the plate boundaries, with a width of d_e and a depth of z_e.

This mesh resolution has been tested to be sufficiently fine as not to affect the model solutions, while keeping the computational cost at acceptable level.

Using the configuration described above, we tested nine transform fault systems (Table 1), with transform length ranging from 70 to 160 km, and half-slip rate ranging from 1.1 to 7.45 cm/yr. The difference in RMBA data between the transform faults and adjacent ridge segment ($\Delta RMBA_{T-R}$) are given by *Gregg et al.*, [2007], and will be used to constrain the model input parameters.

Conservation of mass, momentum, and energy are expressed by:

$$\nabla \cdot \mathbf{V} = 0 \tag{1}$$

$$\nabla P = \nabla \cdot \left[\eta\left(\nabla \mathbf{V} + (\nabla \mathbf{V})^{\mathrm{T}}\right)\right] \tag{2}$$

$$\rho c_p (\mathbf{V} \cdot \nabla) T = \nabla \cdot (k \nabla T) \tag{3}$$

where $\mathbf{V}$ is the mantle velocity field, ρ is the density of mantle, η is the mantle viscosity, c_p is the heat capacity, k is the thermal conductivity, P is the pressure, and T is the temperature. The variables and parameters used in this study are compiled with units and values in Table 2. This set of equations describes the mantle as an incompressible material, and neglects the thermal and mechanical effects of melting and related mantle porosity. Density is constant throughout the model. Therefore, we ignore the possibility of buoyancy-driven upwellings and focus on plate-driven flow. Although upwellings may play an important role at the slower ridges, we will see that this approach is sufficient to explain the global pattern of crustal thickness differences between spreading centers and transform faults.

Mantle viscosity has a significant impact on mantle flow and the temperature field. We adopt the temperature-dependent viscosity with a viscoplastic approximation for brittle weakening following *Behn et al*. [2007] and *Roland et al*. [2010]:

Table 1. Characteristics of the Transform Faults Modeled in This Study[a]

Transform Fault	Ridge System[b]	Approximate Latitude	Half-Slip Rate (cm/yr)	Length (km)	$\Delta RMBA_{T-R}$ (mGals)[c]	ΔH (km)
Garrett	EPR	12°S	7.45	130	−6.0	0.24
Wilkes	EPR	8°S	7.25	100	−7.7	0.31
Siqueiros	EPR	8°N	5.9	150	−13.6	0.54
Clipperton	EPR	10°N	5.75	90	−3.6	0.14
SEIR 1	SEIR	48°S	3.77	135	−8.2	0.33
SEIR 2	SEIR	50°S	3.72	80	−13.2	0.53
Kane	MAR	24°N	1.25	160	6.6	−0.26
Atlantis	MAR	30°N	1.2	70	35.4	−1.41
Hayes	MAR	34°N	1.1	90	13.7	−0.55

[a]Expected crustal thickness differences ΔH are calculated from the difference of residual mantle Bouguer anomaly between the transform and the ridge ($\Delta RMBA_{T-R}$) assuming an oceanic crust density of 2700 kg/m^3 and a mantle density of 3300 kg/m^3 [*Wang et al.*, 2011].
[b]EPR: East Pacific Rise; SEIR: South-East Indian Ridge; MAR: Mid Atlantic Ridge.
[c]From *Gregg et al.* [2007].

© 2015. American Geophysical Union. All Rights Reserved.

Table 2. Parameters and Variables Used in the Study

Name	Symbol	Value	Unit	Equation
Coordinates	x, y, z		km	
Transform length	L	50–350	km	
Mantle velocity	$\mathbf{V}$		$cm \cdot yr^{-1}$	(1) (2) (3)
Pressure	P		Pa	(2)
Temperature	T		°C	(3) (5) (7) (10)
Gravity	g	9.8	$m \cdot s^{-2}$	(6)
Mantle density	ρ	3300	$kg \cdot m^{-3}$	(2) (3) (6)
Effective viscosity	η		Pa·s	(2) (4)
Viscosity (ductile process)	η_T		Pa·s	(4) (5)
Viscosity (brittle process)	η_Y		Pa·s	(4) (6)
Reference viscosity	η_0	10^{19}	Pa·s	(5)
Activation energy	Q	250	$kJ \cdot mol^{-1}$	(5)
Gas constant	R	8.314	$J \cdot mol^{-1} \cdot K^{-1}$	(5)
Mantle potential temperature	T_m	1375	°C	(5)
Cohesion	C_0	10	MPa	(6)
Friction coefficient	μ	0.6	No dimension	(6)
Second invariant of the strain rate tensor	$\dot{\varepsilon}_{II}$		s^{-1}	(6)
Specific heat capacity	c_p	1250	$J \cdot kg^{-1} \cdot K^{-1}$	(3)
Effective thermal conductivity	k		$W \cdot m^{-1} \cdot K^{-1}$	(3) (7)
Reference thermal conductivity	k_0	3	$W \cdot m^{-1} \cdot K^{-1}$	(7)
Nusselt number	Nu	8	No dimension	(7)
Smoothing factor	A_s	0.75	No dimension	(7)
Maximum temperature of hydrothermal circulation	T_{cut}	600	°C	(7)
Maximum depth of hydrothermal circulation	z_{cut}	6	km	(7)
Temperature of permeability barrier	$T_{barrier}$		°C	(8)
Width of melt extraction zone	d_e	2–8	km	
Depth of melt extraction zone	z_e	10–40	km	
Crustal redistribution length	L_f	10–70	km	
Crustal thickness	H		km	(9)
Crustal thickness difference	ΔH		km	(12) (13)
Half-spreading rate	V_p	1.0–7.5	$cm \cdot yr^{-1}$	(9)
Distance along melt trajectories	x_m		km	(9)
Length of a melt trajectory	x_{ml}		km	(9)
Melt flux	f		$km \cdot yr^{-1}$	(9) (10)
Bottom of the melting column	z_b		km	(10)
Top of the melting column	z_t		km	(10)
Melt production rate	p		yr^{-1}	(10) (11)
Melt fraction	F		%	(11)
Critical melt fraction	F_c	1	%	(11)
Relative standard deviation	σ		km	(12)
Degree of constrains	v	15	No dimension	(13)

$$\eta = \min\left(\eta_T, \eta_Y\right) \tag{4}$$

$$\eta_T = \eta_0 \exp\left[\frac{Q}{R}\left(\frac{1}{T} - \frac{1}{T_m}\right)\right] \tag{5}$$

$$\eta_Y = \frac{C_0 - \mu\rho g z}{\sqrt{2}\dot{\varepsilon}_{II}} \tag{6}$$

where η_T is the temperature-dependent viscosity, η_Y is the effective viscosity associated with brittle failure [*Chen and Morgan*, 1990], η_0 is the reference viscosity, Q is the activation energy, R is the gas constant, T_m is the mantle temperature, C_0 is the cohesion, μ is the friction coefficient, g is the gravity acceleration, z is the depth, and $\dot{\varepsilon}_{II}$ is the second invariant of the strain rate tensor. Incorporating this viscoplastic rheology reduces the effective viscosity and induces mantle upwellings in areas with high-strain rate such as the transform domain, leading to elevated temperature and increased melt supply beneath the transform domain [*Behn et al*, 2007].

The thermal structure of mid-ocean ridges is influenced by the hydrothermal circulation of seawater in the cold brittle crust [*Sinha and Evans*, 2004]. As the properties and dynamics of the circulating seawater are poorly constrained [e.g., *Fontaine and Wilcock*, 2007], we adopted the simplified model, originally proposed by *Phipps Morgan et al*. [1987] and *Phipps Morgan and Chen* [1993], that captures the effect of hydrothermal circulation as an enhanced thermal conductivity. Here we used the parameterization of *Phipps Morgan and*

© 2015. American Geophysical Union. All Rights Reserved.

Chen [1993] where hydrothermal circulation is limited to temperatures less than $T_{cut} = 600°C$ and depth less than $z_{cut} = 6$ km and where thermal conductivity decreases exponentially with increasing depth and temperature:

$$k = k_0 + k_0(\mathrm{Nu} - 1)\exp\left[\mathrm{A_s}\left(1 - \frac{T}{T_{\mathrm{cut}}}\right)\right]\exp\left[\mathrm{A_s}\left(1 - \frac{z}{z_{\mathrm{cut}}}\right)\right]/\exp\left(2\mathrm{A_s}\right) \quad (7)$$

where k_0 is the reference thermal conductivity, Nu is the Nusselt number, and A_s is a smoothing factor.

After the mantle flow and thermal structure of the model are solved using COMSOL Multiphysics®, data are exported to MATLAB® to investigate melt trajectory. The extent of melting is a function of temperature, pressure, and the chemical composition of mantle [*Grove et al*., 1992; *Langmuir et al*., 1992]. Here we assume equilibrium batch melting and use the nonlinear anhydrous melting functions proposed by *Katz et al*. [2003], which includes the change of melting rate due to the exhaustion of pyroxene.

After melt is generated, it segregates from the residual solids through porous flow and/or channelized flow [e.g., *Kelemen et al*., 1997]. The rate of melt migration depends on the permeability of the upper mantle [e.g., *Zhu and Hirth*, 2003; *Zhu et al*., 2011]. A recent experimental quantification of mantle permeability using three-dimensional X-ray microtomography leads to an estimation of melt transport velocity in the order of 1 m/yr [*Miller et al*., 2014]. Since the crustal thickness is not directly affected by the melt transport velocity, we ignored the variations in rate of melt migration, and assume melt moves vertically uniformly through mantle before getting to the base of thermal boundary layer, where rapid crystallization of melt facilitates the formation of a permeability barrier [*Sparks and Parmentier*, 1991]. The permeability barrier develops when the decompaction time scale of mantle exceeds the crystallization time scale of melt [*Korenaga and Kelemen*, 1997]. It is associated to the multiple saturation point of plagioclase and pyroxene [*Kelemen and Aharonov*, 1998; *Hebert and Montési*, 2010]. The temperature of the permeability barrier is given approximately by *Montési and Behn* [2007]:

$$T_{barrier} = 1240^{\circ}C + 1.9z \quad (8)$$

where $T_{barrier}$ is the temperature of permeability barrier and z is depth below seafloor in kilometers. Subcrustal reflectors possibly corresponding to the permeability barrier have been recently seismically detected along East Pacific Rise (EPR) at the predicted depth [*Arnoux and Toomey*, 2013].

As the pore space above the permeability barrier is closed, melt accumulates in a decompaction channel that develops at the base of the barrier [*Sparks and Parmentier*, 1991; *Spiegelman*, 1993]. Melt then moves along the barrier toward the ridge axis, where the barrier is shallowest. Fertile heterogeneities in the mantle may perturb the decompaction channel and lead to melt pooling at the base of the lithosphere away from ridge axis [*Katz and Weatherley*, 2012]. We neglect this effect as the amplitude and spatial distribution of mantle heterogeneities is poorly constrained. Since we assume that melt is driven by its buoyancy, melt migration along the permeability barrier will follow the direction of maximum slope [*Magde and Sparks*, 1997], which, in our models focus melt to the ridge axes. Some melt travels laterally to a different ridge segments other than the one closest to where melt was generated. Along the way, it may travel underneath the transform fault, as illustrated in Figure 2 [*Weatherley and Katz*, 2010; *Hebert and Montési*, 2011].

A melt extraction zone (MEZ), where melt is able to penetrate the permeability barrier and get extracted to the surface [*Montési et al*., 2011] is defined around the plate boundaries near the surface. Physically, the MEZ may be associated with the structural damages in the cold, brittle lithosphere, but as we will see, it needs to extend to greater depths. Field observations indicate that diking and fracturing present at mid-ocean ridges and transform faults are possible mechanisms for the melt extraction [*Nicolas*, 1986, 1990; *Kelemen and Dick*, 1995; *Macdonald et al*., 1996; *Perfit et al*., 1996]. Transport along melt-impregnated ductile shear zones [*Kelemen et al*., 1992; *Kaczmarek and Tommasi*, 2011] may play a role at greater depth. We assume here that the MEZ extends from the plate boundaries to an extraction width of d_e, and an extraction depth of z_e (Figure 1). Both parameters are poorly constrained and have been varied systematically in this study. Melt entering MEZ is directly extracted to the surface and accretes to the nearest plate boundary, contributing to the crustal thickness. We assume the MEZ is present along the entire plate boundary system, including transform faults.

© 2015. American Geophysical Union. All Rights Reserved.

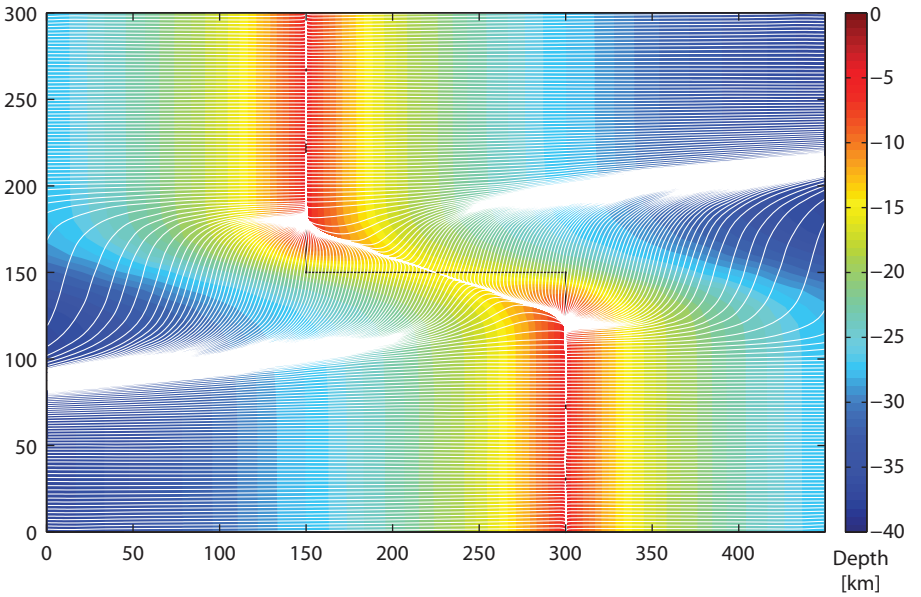

Figure 2. Map of the depth of permeability barrier in the computation domain for the fast-slipping Siqueiros transform (half-slip rate: 5.9 cm/yr, transform length: 150 km). White lines are the trajectories of melt along the barrier. If melt extraction is ignored, some of the melt travels laterally underneath the transform fault to a different ridge segment.

Crustal accretion along the plate boundaries is calculated using the following equations [*Montési et al.*, 2011]:

$$H = \frac{1}{2V_p}\int_0^{x_{ml}} f\, dx_m \tag{9}$$

$$f = \int_{z_b}^{z_t} p\, dz \tag{10}$$

$$p = \begin{cases} 0 & F < F_c \\ \max\left(v_z \dfrac{\partial F}{\partial z}, 0\right), & F \geq F_c \end{cases} \tag{11}$$

where H is the crust accretion, defined as the thickness of crust accreted at each instant along the ridge axis (Figure 3), V_p is the half-spreading rate, f is the melt flux, x_m is the distance along melt trajectories, x_{ml} is the length of each melt trajectory, z_b and z_t are the depth of the bottom and the top of the melting column, p is the melt production rate, F_c is the critical melt fraction representing the retained melt fraction in the mantle [*Kelemen et al.*, 1997; *The MELT Seismic Team*, 1998], and v_z is the velocity of mantle upwelling. Here, we assume $F_c = 1\%$, consistent with estimates of residual melt fractions in the mantle [*McKenzie*, 1985; *The MELT Seismic Team*, 1998]. Changing this parameter has only a minor effect on our calculations.

We applied a smoothing function along the calculated crust accretion profile to represent horizontal redistribution of melt at crustal level along each segment of the plate boundary [*Montési et al.*, 2011]. The smoothing is implemented using the script fastsmooth contributed to MatlabCentral. It processes the data with three passes of a sliding average (boxcar), with a smooth width L_f. We modified the script so that it handles the edges of the signal (the first $L_f/2$ points and the last $L_f/2$ points) with progressively smaller smooth width closer to the end, but no smaller than $L_f/2$. Each segment of the plate boundaries is smoothed separately.

The width of smoothing L_f can be regarded as the distance of lateral dike propagation. We varied this melt redistribution length scale L_f from 10 to 70 km, consistent with geological constrains (see Discussion section 4.2 for detail). With increasing L_f, the crust is averaged along the segment, and the crust accretion close to the transform increases (Figure 3). As will be discussed to a greater extent later, the degree of magmatism

© 2015. American Geophysical Union. All Rights Reserved.

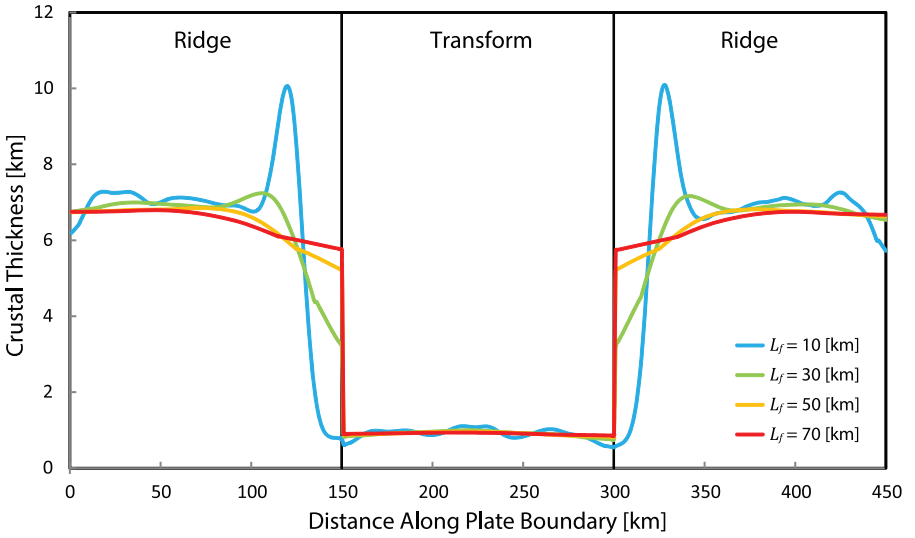

Figure 3. Crustal accretion profile for the fast-slipping Siqueiros transform (half-slip rate: 5.9 cm/yr, transform length: 150 km), with an extraction width of 2 km and an extraction depth of 15 km. The three boxes indicate crust accretion along ridge, transform, and ridge, respectively. Profiles in different colors correspond to different crustal redistribution length L_f. As L_f increases, the crust is more uniform along the ridge segment, and crustal accretion close to the transform increases.

within the transform segment is not sensitive to the variation of L_f. The parameter L_f controls the ridge contribution of crust at transforms. Crustal accretion along the plate boundaries is integrated over time, considering the predefined trajectory of plates away from the ridge axis, to generate maps of crustal thickness over the computation domain (Figure 4).

3. Results

We modeled nine transform fault systems (Table 1), and tested different extraction width d_e, extraction depth z_e, and crustal redistribution length L_f with an idealized ridge-transform-ridge geometry. Each model outputs mantle flow, temperature field, extent of melting, and trajectories of melt along the permeability barrier, and generates maps of crustal thickness over the computation domain. We compiled the model results and studied the influences of spreading rate on the crustal thickness variations.

Two examples of crustal thickness maps are shown in Figure 4. The upper one is for the slow-slipping Atlantis transform (half-slip rate: 1.2 cm/yr, transform length: 70 km), and the lower one is for the fast-slipping Siqueiros transform (half-slip rate: 5.9 cm/yr, transform length: 150 km). The results shown here are for an extraction width d_e of 2 km, an extraction depth z_e of 15 km, and a crustal redistribution length L_f of 60 km.

In both cases, the average crustal thickness for most of the seafloor is about 6–7 km, in agreement with the global trend of oceanic crust [*Chen*, 1992; *White et al*., 1992; *Wang et al*., 2011]. Along the ridge segments, crustal accretion decreases close to the transform fault (Figure 3) due to the cooling effect of the transform offset, sometimes called the "transform fault effect" [*Phipps Morgan and Forsyth*, 1988]. At the slow-slipping transform (Figure 4a), the "transform fault effect" results in a minimum of crustal thickness along the transform fault and associated fracture zones.

Thickened crust is generated along the fast-slipping transform (Figure 4b). Although the "transform fault effect" results in a minimum in the crustal thickness along the ridge as it meets the transform fault, crustal thickness increases in the spreading direction from the inner corner of ridge-transform intersection to the tips of the fracture zone. The thickened crust is due to crustal accretion along the transform (Figure 3), which accumulates on the plate as it is rafted away from the spreading center. By contrast, no crust is accreted along the slow-slipping transform fault (Figure 4a).

To quantitatively evaluate the model results, we define two ridge domains and one transform domain as 20 km wide swaths along plate boundaries centered at ridge axes and transform faults. The width of the

© 2015. American Geophysical Union. All Rights Reserved.

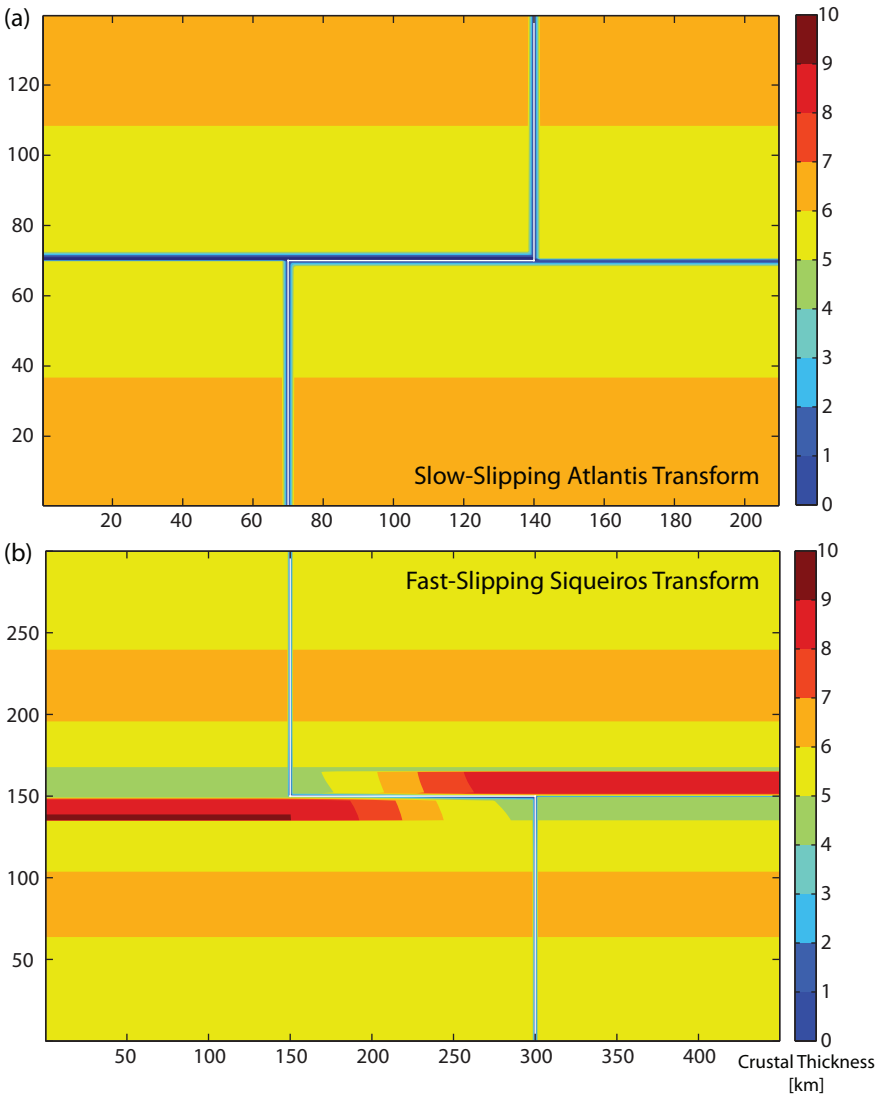

Figure 4. Maps of crustal thickness for the slow-slipping Atlantis transform (half-slip rate: 1.2 cm/yr, transform length: 70 km) and the fast-slipping Siqueiros transform (half-slip rate: 5.9 cm/yr, transform length: 150 km). A crustal redistribution length of 50 km, an extraction width of 2 km and an extraction depth of 15 km are used. In both cases, the average crustal thickness for most area of the seafloor is about 6–7 km. Thickened crust develops along the fast-slipping transform with crustal thickness increases from the inner corner of ridge-transform intersection to the tips of the fracture zone, whereas no thickening occurs at the slow-slipping transform.

swaths is set to account for the resolution of RMBA inversions, which is about 20–25 km [*Sandwell and Smith*, 1997]. We average the crustal thickness in the transform and ridge domains of our model and define the crustal thickness difference ΔH as the difference between averaged crustal thickness in the transform domain, H_T, and in the ridge domain, H_R. A similar measure can be evaluated from the RMBA reported by *Gregg et al*., [2007].

A chi-square (χ^2) analysis [*Press et al*., 2007] is used to estimate the goodness of fit between the model results and the observation for the nine transform fault systems investigated:

$$\chi^2 \sum_{i=1}^{9} \left(\frac{\Delta H_i^{\text{model}} - \Delta H_i^{\text{obervation}}}{\sigma} \right)^2 + \sum_{i=1}^{9} \left(\frac{H_{R_i}^{\text{model}} - H_{R_i}^{\text{obervation}}}{\sigma} \right)^2 \tag{12}$$

Ideally, σ would be the standard error on the observations. However, this quantity is not reported by *Gregg et al*. [2007]. Therefore, we use instead a relative standard error, estimated from the best fit [*Press et al*., 2007]:

© 2015. American Geophysical Union. All Rights Reserved.

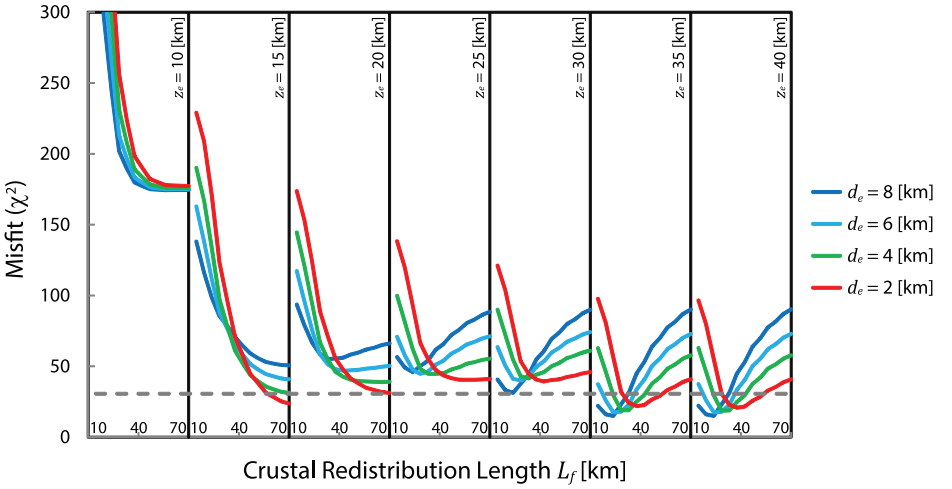

Figure 5. Misfit (χ2) for models with varying melt extraction width d_e, melt extraction depth z_e, and crustal redistribution length L_f. Different colors represent model result with different melt extraction width. Each box contains results for a different melt extraction depth. Crustal redistribution length increases in each box. The dashed gray line shows the χ2 corresponding to a significance level of 0.5%.

$$\sigma^2 = \frac{1}{\nu}\min\left[\sum_{i=1}^{9}\left(\Delta H_i^{\text{model}} - \Delta H_i^{\text{observation}}\right)^2 + \sum_{i=1}^{9}\left(H_{R_i}^{\text{model}} - H_{R_i}^{\text{observation}}\right)^2\right] \quad (13)$$

where ν is the degree of freedom. As we have two observations, H_R and ΔH for each of nine study areas, and we vary three parameters (d_e, z_e, and L_f), $\nu = 9 \times 2 - 3 = 15$. Two sets of constraints are used: the ΔRMBA-converted crustal thickness difference $\Delta H^{\text{observation}}$ (assuming an average oceanic crust density of 2700 kg/m^3 and a mantle density of 3300 kg/m^3 [*Wang et al*., 2011]) and the reference thickness of oceanic crust $H_R^{\text{observation}}$ (7.1 km [*White et al*., 1992]).

A range of values for the extraction width d_e (2–8 km), extraction depth z_e (10–40 km), and crustal redistribution length L_f (10–70 km) have been tested in the models. The resulting χ^2 values are plotted over the parameter space, as shown in Figure 5. Models with the minimum χ^2 values fit the observation best.

For models with small values of extraction depth and extraction width, χ^2 decreases with increasing crustal redistribution length. However, for larger extraction depth and width, χ^2 increases for the longest crustal redistribution length.

Several combinations of parameters produce acceptable models, using a χ^2 significance level of 0.5% (corresponding to a χ^2 value of 30.578). Acceptable models can be categorized into two groups. The first group has smaller values for extraction width and depth (d_e: 2–4 km, z_e: 15–20 km), and larger crustal redistribution length (L_f: 50–70 km). The second group has larger values for extraction width and depth ($d_e > 4$ km, $z_e > 35$ km), but smaller crustal redistribution length (L_f: 15–45 km). Neither group can be favored from purely statistical arguments. However, the first group is most consistent with geological observations, as discussed in the next section.

To better understand the physical difference between the two groups of parameter combinations, we examined the crustal accretion profiles for models in each group (Figure 6). For models with fast slip rate, both groups feature melt extraction along the transform faults (Figure 6b). However, for slow-slipping models with the first group of parameters, no melt is extracted along the transforms, whereas for models with the second group of parameters, melt extraction occurs along the slow-slipping transform (Figure 6a). Both groups of parameters satisfy equally well the observed slip-rate-dependent RMBA variations between ridge and transform domains and produce realistic crustal thicknesses. The major difference lies in, whether melt extraction is possible along the slow-slipping transforms.

4. Discussion

4.1. Melt Extraction at Slow-Slipping Transform Faults?

To find out if melt extraction at slow-slipping transform faults is possible, we looked into the geological, geochemical, and seismic observations at oceanic transform faults. Little evidence can be found supporting

© 2015. American Geophysical Union. All Rights Reserved.

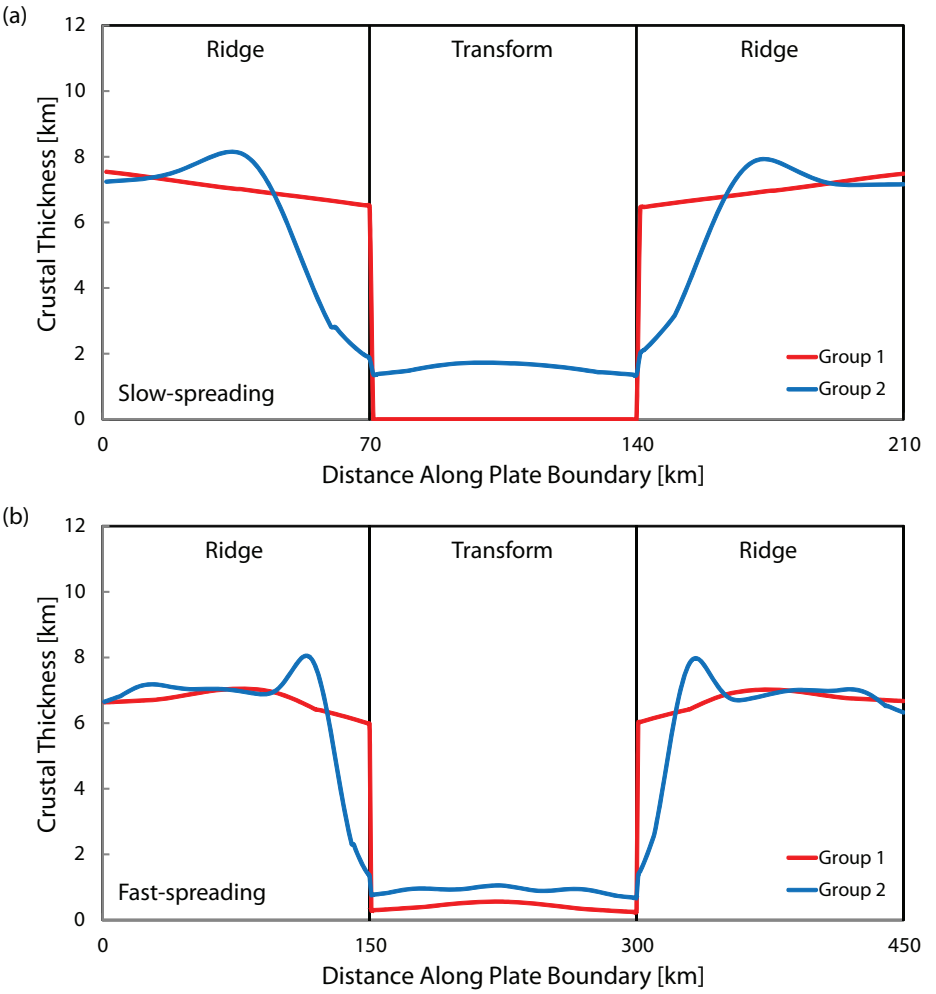

Figure 6. Crustal accretion profiles for models with the first group of parameters (in red, d_e: 2–4 km, z_e: 15–20 km, L_f: 50–70 km) and the second group of parameters (in blue, d_e: > 4 km, z_e > 35 km, L_f: 15 – 45 km), for a) slow- (half-slip rate: 1.2 cm/yr) and b) fast-slipping transforms (half-slip rate: 5.9 cm/yr). Both groups have melt extraction along the fast-slipping transform faults. However, for the first group of parameters, no melt is extracted along the slow-slipping transforms, while for the second group of parameters, melt extraction occurs along the slow-slipping transform.

magmatism at slow-slipping transforms. Therefore, the first group of acceptable models appears more geologically realistic than the second group.

Magmatism at fast-slipping to intermediate-slipping transforms has been discussed in a number of geological studies. For example, at the fast-spreading East Pacific Rise, bathymetric surveys, dredging and submersible dives have discovered constructional volcanic mounds and fresh lavas in the troughs of the Clipperton transform [*Kastens et al.*, 1986], the Siqueiros transform [*Perfit et al.*, 1996], the Garrett transform [*Hékinian et al.*, 1992], the Terevaka transform [*Constantin et al.*, 1996], and the Raitt transform [*Castillo et al.*, 1998]. Fresh basalts have also been found along the intermediate-slipping Blanco transform [*Gaetani et al.*, 1995]. By contrast, magmatic activity is sparsely reported at slow-slipping transforms, which are instead dominated by exposures of serpentinized peridotite [*Thompson and Melson*, 1972] or thin and weathered basalt layer on top of transform valley flanks [*Auzende et al.*, 1989; *Bonatti et al.*, 2003], implying that melt extraction seldom occurs there.

Besides, lavas erupted along fast-slipping transform faults are generally more primitive and more porphyritic than lavas from the nearby ridge axes [*Perfit et al.*, 1996; *Castillo et al.*, 1998; *Wendt et al.*, 1999]. This suggests that magma in the transform is extracted directly and rapidly to the surface, and no crustal processes in magma chambers are involved [*Fornari et al.*, 1989; *Hékinian et al.*, 1995]. They underwent a different cooling history from lava erupted along the spreading center. By contrast, basalts collected at slow-slipping

© 2015. American Geophysical Union. All Rights Reserved.

transform faults have MgO content at the same level as the samples recovered from the adjacent ridge axes [*Lawson et al*., 1996; *Bryan et al*., 1981], implying the crust at slow-slipping transforms is created at the associated ridge segment, without evidence for a different crystallization history that would represent magmatism along the transforms.

Melt extraction processes at oceanic transform faults can also be reflected in seismic activity. Teleseismic data indicate different kinds of earthquakes at fast-slipping and slow-slipping transforms. Studies of earthquake scaling relations for oceanic transform faults demonstrate that the seismic coupling coefficient, defined as the ratio between the observed and expected seismic moment [*Pacheco et al*., 1993] is about 0.15, implying that nearly 85% of the fault slip is aseismic [*Boettcher and Jordan*, 2004]. Aseismic phenomenon can be accounted for by creep events [*Wesson*, 1988], slow and silent earthquakes [*Beroza and Jordan*, 1990; *Miller et al*., 2002], all of which are typically attributed to fault weakening resulted from changes of fluid pressure [*Obara et al*., 2004; *Kodaira et al*., 2004; *Becken et al*., 2011]. Magma injection and eruption along transform faults may lead to elevated fluid pressures that weaken the faults [*Vidale and Shearer*, 2006; *Becken et al*., 2011]. If melt is extracted along fast-slipping transforms, but not at slow-slipping transforms, we should expect fast-slipping transforms to be more aseismic than the slow-slipping ones. Previous studies suggest that the seismic coupling coefficient decreases with increasing slip rate, with more aseismic slip at fast-slipping transforms than at slow-slipping transforms [*Kawasaki et al*., 1985; *Rundquist and Sobolev*, 2002]. This trend is in agreement with our prediction.

However, *Boettcher and Jordan* [2004] argue that seismic coupling coefficient does not decrease significantly with increasing slip rate. They do not identify a systematic relation between seismic coupling coefficient and slip rate. These conflicting conclusions may result from the large spatial variability of seismicity within the transforms, which is ignored in some studies [e.g., *Rundquist and Sobolev*, 2002], but kept in the recent one [*Boettcher and Jordan*, 2004]. Earlier studies may have underestimated the seismic coupling coefficient for two reasons: (1) they use data from the Harvard Centroid Moment Tensor (CMT) catalog and the International Seismological Center (ISC) online bulletin, which have short-catalog duration ($\sim$36 years) that may not be sufficient to span the long earthquake cycles at slow-slipping transforms ($>$ 60 years, assuming a stress drop $>$ 10 MPa [*Boettcher and McGuire*, 2009]); (2) they use a half-space cooling model to calculate the temperature limit of seismicity. More realistic thermal models incorporating a viscoplastic rheology, non-Newtonian viscous flow and the effects of shear heating and hydrothermal cooling lead to a smaller seismogenic area [*Liu et al*., 2012]. These effects are more pronounced for the slow-slipping transforms. Taking these effects into account, it is possible that the seismic coupling coefficient is actually higher at slow-slipping transform than at fast-slipping transforms, implying that slow-slipping transforms are at least less magmatic than the fast-slipping ones.

The differences in seismic behavior between fast-slipping and slow-slipping transform faults are better illuminated through microearthquake experiments conducted at different mid-ocean ridge systems. At the fast-spreading East Pacific Rise, an array of autonomous underwater hydrophones in the vicinity of the Clipperton transform fault recorded a cluster of earthquakes associated with dike intrusion and propagation [*Dziak et al*., 2009]. At the Blanco transform, Juan de Fuca Ridge, low-frequency, periodic tremor-like signals, and earthquake swarms are also documented, and interpreted to be of volcanic origin, which has been confirmed by ocean-bottom photographs and water column data [*Dziak et al*., 1996]. By contrast, at the slow-spreading Mid-Atlantic Ridge, earthquakes along the Kane transform [*Wilcock et al*., 1990] and Oceanographer transform [*Cessaro and Hussong*, 1986] detected by ocean bottom seismometers show focal mechanisms of normal faulting, indicating differential lithospheric extension across the transform faults, caused by a deficit of magmatism [*Cessaro and Hussong*, 1986]. Besides, a recent 4 year hydroacoustic monitoring of seismicity at northern Mid-Atlantic Ridge between $\sim$15°N and $\sim$35°N [*Smith et al*., 2002; *Smith et al*., 2003] did not record microearthquakes with the characteristics of magmatic activities along the transforms (Deborah K. Smith, personal communication, 2013). Although seismic behavior is complicated by the stress state and material property of each individual transform faults, generally speaking, most seismic events at slow-slipping transforms have a tectonic origin, while seismicity at fast-slipping transforms mainly reflects magmatic processes [*Rundquist and Sobolev*, 2002]. The distinct patterns of earthquakes at transform faults with varying slip rate indicate that melt extraction occurs along the fast-slipping transforms, but not at slow-slipping ones.

4.2. Preferred Parameters for Melt Extraction

As melt extraction along slow-slipping transform is unlikely to take place, we consider that the first group of acceptable models, i.e., those with melt extraction width d_e between 2 and 4 km, melt extraction depth z_e

© 2015. American Geophysical Union. All Rights Reserved.

between 15 and 20 km, and crustal redistribution length L_f between 50 and 70 km, are the most realistic. The dimensions of MEZ and crustal redistribution implied by these models are supported by several observations.

At mid-ocean ridges, neovolcanic activity is typically confined within about 2 km of the ridge axis [*Macdonald*, 1982], in agreement with our preferred value for melt extraction width between 2 and 4 km. Broader melt extraction zones may be appropriate at ultraslow-spreading center [*Standish and Sims*, 2010], which, as they lack transform offsets [*Dick et al*., 2003], are not considered in this study.

Our preferred extraction depth between 15 and 20 km implies that extraction of melts in the ridge and transform domains mainly occurs through fractures and shear zones in the lithosphere. The depth of fracturing can be assessed from the maximum depth of earthquakes at transform faults. Ocean bottom seismometer studies [e.g., *Wilcock et al*., 1990], teleseismic inversions [e.g., *Abercrombie and Ekström*, 2001], and laboratory extrapolation [e.g., *Boettcher et al*., 2007] suggest that the seismicity at transform faults is limited by the location of 600°C isotherm, and extends to a depth of ~20 km [*Bergman and Solomon*, 1988; *Abercrombie and Ekström*, 2001; *Schlindwein et al*., 2013].

Thus fractures provide a plausible way for melt to penetrate the lithosphere, and our preferred values for melt extraction depth are supported. On the one hand, since in the model we neglected the latent heat of crystallization of melt, which impacts the thermal structure [*Katz*, 2008] and thins the thermal boundary layer, the actual extraction zone could be shallower than inferred here; On the other hand, the buoyancy-driven mantle flow neglected in this study may have an effect for ridges spreading slower than 1 cm/yr, thin the lithosphere underneath the ridges, focus melt away from the transforms and deepen the melt extraction zone. If the melt extraction occurs through fractures, the extraction depth probably depends on the thickness of the brittle layer and varies with spreading rate and lateral locality. Slow-slipping transforms may have deeper MEZs, and the extraction depth for fast-slipping transforms may be relatively shallower (see Discussion section 4.3 for detail). Our models are not sensitive to these variations as long as the permeability barrier and the MEZ intersect and we use one uniform extraction depth for simplicity. Furthermore, mantle exposures at ophiolites show that melt is typically associated with shear zones [*Kelemen et al*., 1992; *Kaczmarek and Müntener*, 2008; *Kaczmarek and Tommasi*, 2011]. Therefore, melt extraction enhanced by deformation processes can continue throughout the lithosphere.

The crustal redistribution length can be constrained by the observations of lateral dike propagation, which has been documented in Iceland [*Einarsson and Brandsdottir*, 1978], in Hawaii [*Klein et al*., 1987], on the Juan de Fuca Ridge [*Fox et al*., 1995; *Dziak et al*., 1995], and on the East Pacific Rise [*Dziak et al*., 2009]. The observed lateral dike propagation distances vary, but most of them exceeds 30 km. Along the CoAxial segment, Juan de Fuca Ridge, a swarm of earthquakes migrated more than 60 km along the axis [*Dziak et al*., 1995]. At the East Pacific Rise, 9°50′N, regional seismicity reflected a lateral dike intrusion event with a propagation distance of 25–40 km [*Dziak et al*., 2009]. The length scale of crustal redistribution is controlled by the width, thermal state, and pressure gradient of propagating dikes. Thermodynamic models of lateral dike propagation show that, with a width of 1.5 m, a constant pressure drop of 5 MPa and a temperature of 1200°C, magma can travel in cold host rocks (temperature: 0–500°C) for more than 50 km before freezing [*Fialko and Rubin*, 1998]. Thus, our preferred crustal redistribution length between 50 and 70 km is geologically plausible. Besides, even with such large melt redistribution length scale, along-axis variations of crustal thickness are preserved in our models, as is observed at both fast-spreading and slow-spreading ridges [*Lin et al*., 1990; *Canales et al*., 2003].

4.3. Expectations for Global Systematics

With the preferred values for melt extraction width and crustal redistribution length, we systematically vary slip rate, transform length, and melt extraction depth to understand the systematic variation in crustal thickness between transform domain and ridge domain that may be expected at locations other than the nine examples analyzed by *Gregg et al*. [2007].

The relationship between crustal thickness difference and spreading rate for models with a transform length of 150 km, a crustal redistribution length of 50 km, an extraction width of 2 km, and varying extraction depths is shown in Figure 7a. The crustal thickness difference varies with spreading rate, and changes

© 2015. American Geophysical Union. All Rights Reserved.

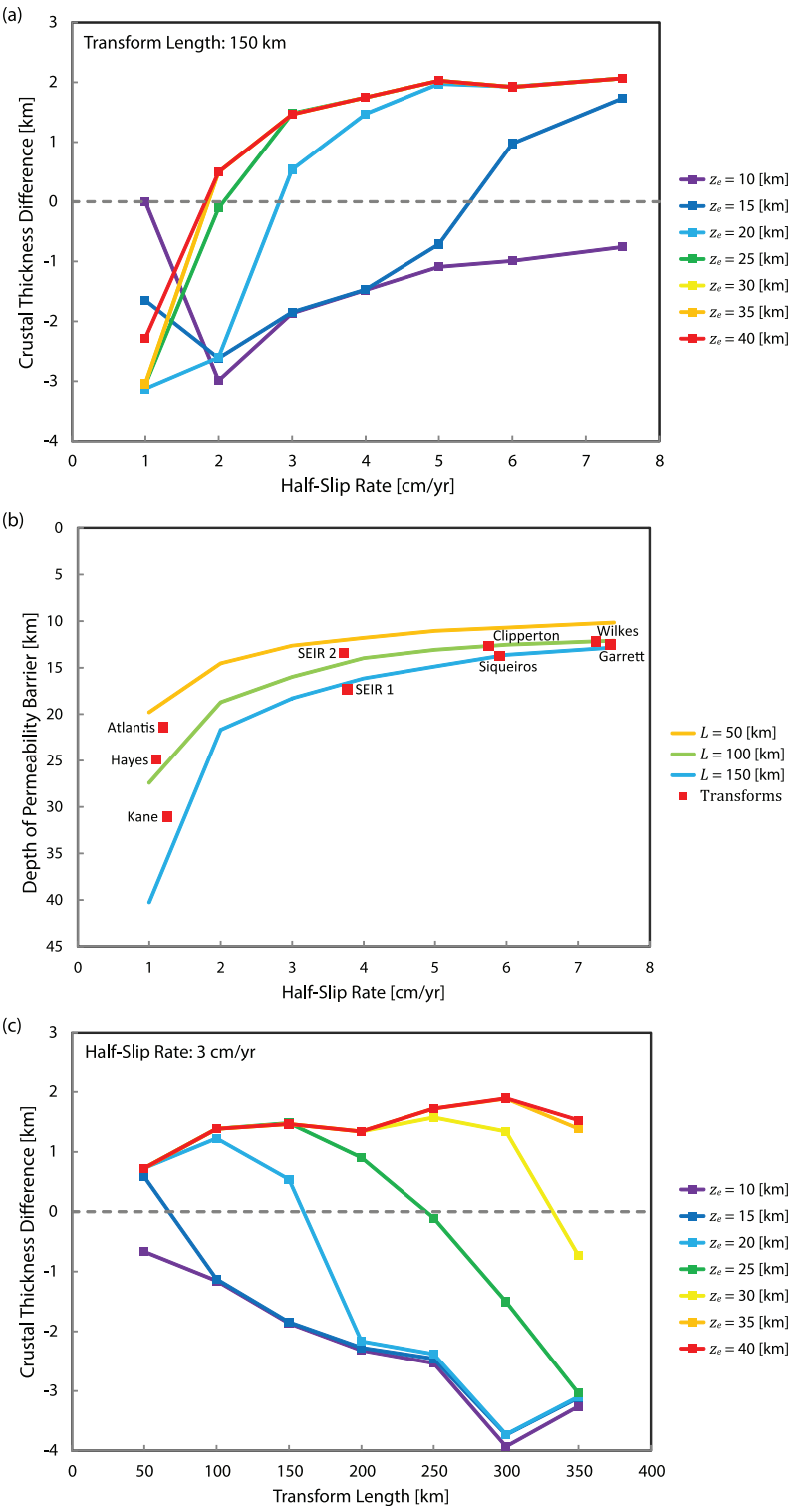

Figure 7. (a) Relationship between crustal thickness difference and spreading rate for a transform length of 150 km. (b) Relationship between depth of permeability barrier at the center of the transform and half-slip rate. Lines in yellow, green, and blue are results from models with transform length of 50, 100, and 150 km, respectively. Red squares are results from models with specific geometry of the indicated transforms. (c) Relationship between crustal thickness difference and the length of transform for a half-slip rate of 3 cm/yr. Different colors represent results with different melt extraction depth. An extraction width of 2 km and a crustal redistribution length of 50 km are used throughout.

© 2015. American Geophysical Union. All Rights Reserved.

from negative at slow-spreading ridges, to positive at fast-spreading ridges (except for $z_e = 10$ km, with which the transform faults cannot accumulate thicker crust than the adjacent ridges, even the fast-slipping ones). In other words, intermediate-slipping and fast-slipping transforms accumulate thicker crust than the associated ridges, while no thickening is present at slow-slipping transforms. The extraction depth controls the spreading rate at which crustal thickness changes from negative to positive. The variations of crustal thickness difference at half-spreading rate between 1 and 4 cm/yr reflect the spatial relationship between permeability barrier and MEZ (Figure 7b). The transition from nonintersection to intersection between MEZ and permeability barrier beneath a transform fault occurs between half-slip rate of 1 and 4 cm/yr. At extraction depth less than 10 km, magma cannot be fully extracted, resulting in oceanic crust thinner than the general estimation. Depending on the transform length, at extraction depth between 15 and 20 km, the MEZ cuts the permeability barrier at fast-slipping transforms, but not at slow-slipping ones. And at extraction depth larger than 35 km, the MEZ penetrates the permeability barrier everywhere in the domain despite the slip-rate. To satisfy the RMBA observation, at slow-slipping transforms, the melt extraction depth can be as deep as 30 km, while at fast-slipping transforms, the extraction depth may vary from 15 to 20 km. Once the MEZ fully intersects the permeability barrier, crustal thickness differences become stable and are no longer affected by the spreading rate.

Figure 7c shows the relationship between crustal thickness difference and transform length for models with half-spreading rate of 3 cm/yr, a crustal redistribution length of 50 km, an extraction width of 2 km, and different extraction depths. For melt extraction depth smaller than 20 km, the crustal thickness difference decreases with increasing length of transform. For melt extraction depth larger than 15 km, the crustal thickness difference increases with increasing length of transform at short transforms, and may decrease for the longest transforms. Increasing the extraction depth increases the transform length for which the maximum crustal difference is obtained. The small value of crustal thickness difference at short offset is a combination of the small temperature anomaly associated with the transform and a lack of time for crust to accumulate along the transform fault. The reduced crustal thickness difference at long offset is due to the decreased melt production and greater depth of the permeability barrier beneath the transform as conductive cooling becomes dominant. The width of the partial melting region in the upper mantle could be as wide as 200 km at fast-spreading ridges and as narrow as 50 km at slow-spreading ridges [*Chen*, 2000]. Therefore, when the transform fault is long enough, the partial melting regions beneath two adjacent ridge segments may be isolated, and no cross-segment melt transport may occur, resulting in an absence of magmatic activities in the transform domain.

4.4. Mechanisms for Magmatism at Fast-Slipping Transform Faults

Magmatic activity at fast-slipping transform faults has been attributed to both "leaky" transforms [*Menard and Atwater*, 1969] and ITSCs [*Fornari et al*., 1989]. In most cases, magmatic transforms are transtensional due to the plate reorientation [e.g., *Thompson and Melson*, 1972; *Hékinian et al*., 1992; *Perfit et al*., 1996; *Dziak et al*., 1996] and feature ITSCs [e.g., *Fornari et al*., 1989; *Hékinian et al*., 1992]. Young lava flows are found in the pull-apart basins and in the vicinity of the ITSCs. However, along some transforms such as Siqueiros and Garrett, fresh basaltic rocks are also present on the transform floor and intratransform wall away from ITSCs [*Perfit et al*., 1996; *Tepley et al*., 2004]. In addition, crustal thickening and volcanism at the transpressional Clipperton transform [*Pockalny*, 1996] cannot be easily explained by the "leaky" transform concept or ITSCs. Melt extraction at transforms is more universal than transtension or ITSCs. Our models assume melt extraction occurs regardless of tectonic environment, although it is likely that transtension makes melt extraction easier.

While three-dimensional melt migration and extraction is the focus of our study, this mechanism is not incompatible with leaky transforms and ITSCs. Plate reorientation not only induces transtensional forces that create leaky transforms and ITSCs, it may also enhance structural damages at transforms [*Menard and Atwater*, 1969], which may facilitate the formation of the melt extraction zone. This damage is expected at both transpressional and transtensional faults, although more so in the latter case. Additionally, migration of ridge may lead to asymmetric melt production beneath the leading and trailing plates, contributing to the crustal thickness variation at segmented mid-ocean ridges [*Carbotte et al*., 2004].

In general, melt extraction at ridge-transform systems can be complicated by changes of plate motions, and magmatic activity at fast-slipping transform faults may result from the combined effects of "leaky" transform, ITSCs, and three-dimensional melt migration and extraction processes.

© 2015. American Geophysical Union. All Rights Reserved.

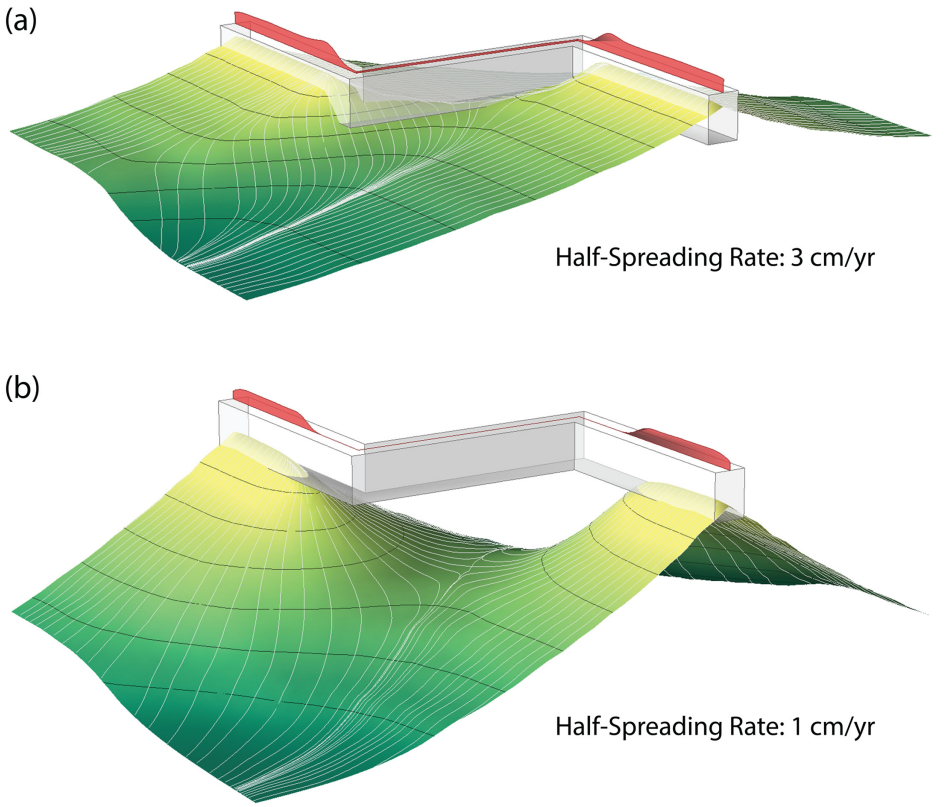

Figure 8. Spatial relationship between permeability barrier and melt extraction zone for (a) a fast-spreading ridge (half-spreading rate: 3 cm/yr) and (b) a slow-spreading ridge (half-spreading rate: 1 cm/yr) with a transform length of 150 km. The curved surface represents the permeability barrier with 5 km depth contours (black) and color-coded with depth (yellow to green from shallow to deep). White lines on the permeability barrier surface are melt trajectories. White boxes are the melt extraction zones. The red areas on top of melt extraction zones indicate melt flux at surface. At fast-slipping transform (a), the permeability barrier intersects with the melt extraction zone and melt can be extracted along the transform. At slow-slipping transform (b), the permeability barrier does not intersect with the melt extraction zone and no melt is extracted along the transform fault.

4.5. Geochemical Segmentation at Fast-Spreading Ridges

Melt extraction at transform faults may provide a new explanation for geochemical segmentation (or, "transform discontinuities"). Geochemical segmentation refers to different ridge segments offset by transforms or nontransform discontinuities having distinct signatures in major elements, trace elements, and isotopic chemistry [*Schilling et al.*, 1982; *Machado et al.*, 1982; *Langmuir and Bender*, 1984; *Thompson et al.*, 1985; *Langmuir et al.*, 1986]. This phenomenon is most prominent at fast-spreading ridges, where even nontransform discontinuities impart geochemical segmentation [*Langmuir et al.*, 1986], whereas at slow-spreading ridges, geochemical segmentation is more ambiguous [e.g., *Batiza et al.*, 1988; *Langmuir et al.*, 1992; *Reynolds and Langmuir*, 1997].

According to our models, fast-slipping transform faults act as an easy pathway for magma to erupt. Therefore, they prevent cross-segment transportation of melt. Only a limited amount of melt can travel beneath the inactive fracture zone outside the transform domain (Figure 2). On this basis, at fast-spreading ridges, low degree of mixing is expected for melts from different ridge segments with different source composition, and any original heterogeneity can be preserved and reflected at each segment. By contrast, at slow-spreading ridges, melt travels along the permeability barrier across the transform fault without being extracted in the transform domain, extensive mixing of melts between segments is possible. Melts with different compositions are homogenized, resulting in less obvious geochemical segmentation.

5. Conclusions

In summary, whether melt is extracted along oceanic transform faults depends on the slip rate of the transforms. At fast-spreading and intermediate-spreading ridges, the MEZ intersects the permeability barrier

© 2015. American Geophysical Union. All Rights Reserved.

underneath transform faults. Melt extraction occurs along the transforms, resulting in thickened crust in the transform domain. By contrast, beneath slow-slipping transforms, the MEZ does not intersect the permeability barrier, no melt is extracted in the transform domain, so the crust there is thin (Figure 8). The melt extraction zone is estimated to be about 2–4 km wide, 15–20 km deep. Crustal thickness is smoothed over a length scale of 50–70 km reflecting along-axis dike propagation at crustal level.

Melt extraction occurs mainly through fracturing in the lithosphere near plate boundaries, with possible extensions in ductile shear zones, and may be complicated by changes in plate motions. Magmatism at fast-slipping transform faults may be a result of "leaky" transform, ITSCs, three-dimensional transport of melt toward transforms, or the combination of the three. Fast-slipping and slow-slipping transform faults exhibit different degree of magmatic activities, and the difference can be reflected in geological features, geochemical signals, and seismic behavior at transform faults. Melt extraction along transforms may also provide a possible explanation for geochemical segmentation observed at fast-spreading ridges.

Acknowledgements

This work is supported by the National Science Foundation under the grant OCE-0937277. We thank Deborah K. Smith for her insight on ridge processes, and Tom O'Haver for contributing his routine fastsmooth to MatlabCentral (http://www.mathworks.com/matlabcentral). This manuscript was improved by constructive reviews by Yongshun J. Chen, Richard F. Katz and Roger C. Searle. COMSOL Multiphysics® is a registered trademark of COMSOL AB. Models and scripts related to this study will be provided upon request.

References

Abercrombie, R. E., and G. Ekström (2001), Earthquake slip on oceanic transform faults, *Nature*, *410*, 74–77, doi:10.1038/35065064.

Arnoux, G. M., and D. R. Toomey (2013), Observations of anomalous subcrustal reflections along the East Pacific Rise: Possible detection of a melt permeability barrier, Abstract OS43A-1883 presented at 2013 Fall Meeting, AGU, San Francisco, Calif., 9–13 Dec.

Auzende, J.-M., D. Bideau, E. Bonatti, M. Cannat, J. Honnorez, Y. Lagabrielle, J. Malavieille, V. Mamaloukas-Frangoulis, and C. Mevel (1989), Direct observation of a section through slow-spreading oceanic crust, *Nature*, *337*, 726–729, doi:10.1038/337726a0.

Batiza, R., W. G. Melson, and T. O'Hearn (1988), Simple magma supply geometry inferred beneath a segment of the Mid-Atlantic Ridge, *Nature*, *335*, 428–431, doi:10.1038/335428a0.

Becken, M., O. Ritter, P. A. Bedrosian, and U. Weckmann (2011), Correlation between deep fluids, tremor and creep along the central San Andreas fault, *Nature*, *480*, 87–90, doi:10.1038/nature10609.

Behn, M. D., M. S. Boettcher, and G. Hirth (2007), Thermal structure of oceanic transform faults, *Geology*, *35*, 307–310, doi:10.1130/G23112A.1.

Bergman, E. A., and S. C. Solomon (1988), Transform fault earthquakes in the North Atlantic: Source mechanisms and depth of faulting, *J. Geophys. Res.*, *93*, 9027–9057, doi:10.1029/JB093iB08p09027.

Beroza, G. C., and T. H. Jordan (1990), Searching for slow and silent earthquakes using free oscillations, *J. Geophys. Res.*, *95*, 2485–2510, doi:10.1029/JB095iB03p02485.

Boettcher, M. S., and T. H. Jordan (2004), Earthquake scaling relations for mid-ocean ridge transform faults, *J. Geophys. Res.*, *109*, B12302, doi:10.1029/2004JB003110.

Boettcher, M. S., and J. J. McGuire (2009), Scaling relations for seismic cycles on mid-ocean ridge transform faults, *Geophys. Res. Lett.*, *36*, L21301, doi:10.1029/2009GL040115.

Boettcher, M. S., G. Hirth, and B. Evans (2007), Olivine friction at the base of oceanic seismogenic zones, *J. Geophys. Res.*, *112*, B01205, doi:10.1029/2006JB004301.

Bonatti, E., M. Ligi, D. Brunelli, A. Cipriani, P. Fabretti, V. Ferrante, L. Gasperini, and L. Ottolini (2003), Mantle thermal pulses below the Mid-Atlantic Ridge and temporal variations in the formation of oceanic lithosphere, *Nature*, *423*, 499–505, doi:10.1038/nature01594.

Bryan, W. B., G. Thompson, and J. N. Ludden (1981), Compositional variation in normal MORB from 22°–25°N: Mid-Atlantic ridge and Kane fracture zone, *J. Geophys. Res.*, *86*, 11,815–11,836, doi:10.1029/JB086iB12p11815.

Canales, J. P., R. S. Detrick, D. R. Toomey, and W. S. Wilcock (2003), Segment-scale variations in the crustal structure of 150–300 kyr old fast spreading oceanic crust (East Pacific Rise, 8°15′N–10°5′N) from wide-angle seismic refraction profiles, *Geophys. J. Int.*, *152*, 766–794, doi:10.1046/j.1365-246X.2003.01885.x.

Carbotte, S. M., C. Small, and K. Donnelly (2004), The influence of ridge migration on the magmatic segmentation of mid-ocean ridges, *Nature*, *429*, 743–746, doi:10.1038/nature02652.

Castillo, P. R., J. H. Natland, Y. Niu, and P. F. Lonsdale (1998), Sr, Nd and Pb isotopic variation along the Pacific–Antarctic risecrest, 53–57°S: Implications for the composition and dynamics of the South Pacific upper mantle, *Earth Planet. Sci. Lett.*, *154*, 109–125, doi:10.1016/S0012–821X(97)00172-6.

Cessaro, R. K., and D. M. Hussong (1986), Transform seismicity at the intersection of the oceanographer fracture zone and the Mid-Atlantic Ridge, *J. Geophys. Res.*, *91*, 4839–4853, doi:10.1029/JB091iB05p04839.

Chen, Y. J. (1992), Oceanic crustal thickness versus spreading rate, *Geophys. Res. Lett.*, *19*, 753–756, doi:10.1029/92GL00161.

Chen, Y. J. (2000), Dependence of crustal accretion and ridge axis topography on spreading rate, mantle temperature, and hydrothermal cooling, in *Ophiolites and Oceanic Crust: New Insights from Field Studies and the Ocean Drilling Program, Geol. Soc. Am. Spec. Pap., vol. 349*, edited by Y. Dilek et al., pp. 161–179, Geol. Soc. of Am., Boulder, Colo.

Chen, Y. J., and W. J. Morgan (1990), A nonlinear rheology model for mid-ocean ridge axis topography, *J. Geophys. Res.*, *95*, 17,583–17,604, doi:10.1029/JB095iB11p17583.

Constantin, M., R. Hékinian, D. Bideau, and R. Hébert (1996), Construction of the oceanic lithosphere by magmatic intrusions: Petrological evidence from plutonic rocks formed along the fast-spreading East Pacific Rise, *Geology*, *24*, 731–734, doi:10.1130/0091-7613(1996)024<0731:COTOLB>2.3.CO;2.

Dick, H. J. B., L. Lin, and H. Schouten (2003), An ultraslow-spreading class of ocean ridge, *Nature*, *426*, 405–412, doi:10.1038/nature02128.

Dziak, R. P., C. G. Fox, and A. E. Schreiner (1995), The June–July 1993 seismo-acoustic event at CoAxial segment, Juan de Fuca Ridge: Evidence for a lateral dike injection, *Geophys. Res. Lett.*, *22*, 135–138, doi:10.1029/94GL01857.

Dziak, R. P., C. G. Fox, R. W. Embley, J. E. Lupton, G. C. Johnson, W. W. Chadwick, and R. A. Koshi (1996), Detection of and response to a probable volcanogenic T-wave event swarm on the Western Blanco Transform Fault Zone, *Geophys. Res. Lett.*, *23*, 873–876, doi:10.1029/96GL00240.

© 2015. American Geophysical Union. All Rights Reserved.

Dziak, R. P., D. R. Bohnenstiehl, H. Matsumoto, M. J. Fowler, J. H. Haxel, M. Tolstoy, and F. Waldhauser (2009), January 2006 seafloor-spreading event at 9°50′ N, East Pacific Rise: Ridge dike intrusion and transform fault interactions from regional hydroacoustic data. *Geochem. Geophys. Geosyst.*, *10*, Q06T06, doi:10.1029/2009GC002388.

Einarsson, P., and B. Brandsdottir (1978), Seismological evidence for lateral magma intrusion during the July 1978 deflation of the Krafla volcano in NE-Iceland, *J. Geophys.*, *47*, 160–165, doi:10.2172/890964.

Fialko, Y. A., and A. M. Rubin (1998), Thermodynamics of lateral dike propagation: Implications for crustal accretion at slow spreading mid-ocean ridges. *J. Geophys. Res.*, *103*, 2501–2514, doi:10.1029/97JB03105.

Fontaine, F. J., and W. S. D. Wilcock (2007), Two-dimensional numerical models of open-top hydrothermal convection at high Rayleigh and Nusselt numbers: Implications for mid-ocean ridge hydrothermal circulation, *Geochem. Geophys. Geosyst.*, *8*, Q07010, doi:10.1029/2007GC001601.

Fornari, D. J., D. G. Gallo, M. H. Edwards, J. A. Madsen, M. R. Perfit, and A. N. Shor (1989), Structure and topography of the Siqueiros transform fault system: Evidence for the development of intra-transform spreading centers, *Mar. Geophys. Res.*, *11*, 263–299, doi:10.1007/BF00282579.

Fox, P. J., and D. G. Gallo (1984), A tectonic model for ridge-transform-ridge plate boundaries: Implications for the structure of oceanic lithosphere, *Tectonophysics*, *104*, 205–242, doi:10.1016/0040-1951(84)90124-0.

Fox, C. G., W. E. Radford, R. P. Dziak, T. K. Lau, H. Matsumoto, and A. E. Schreiner (1995), Acoustic detection of a seafloor spreading episode on the Juan de Fuca Ridge using military hydrophone arrays, *Geophys. Res. Lett.*, *22*, 131–134, doi:10.1029/94GL02059.

Gaetani, G. A., S. E. DeLong, and D. A. Wark (1995), Petrogenesis of basalts from the Blanco Trough, northeast Pacific: Inferences for off-axis melt generation, *J. Geophys. Res.*, *100*, 4197–4214, doi:10.1029/94JB02774.

Ghods, A., and J. Arkani-Hamed (2000), Melt migration beneath mid-ocean ridges, *Geophys. J. Int.*, *140*, 687–697, doi:10.1046/j.1365-246X.2000.00032.x.

Gregg, P. M., J. Lin, M. D. Behn, and L. G. J. Montési (2007), Spreading rate dependence of gravity anomalies along oceanic transform faults, *Nature*, *448*, 183–187, doi:10.1038/nature05962.

Gregg, P. M., M. D. Behn, J. Lin, and T. L. Grove (2009), Melt generation, crystallization, and extraction beneath segmented oceanic transform faults, *J. Geophys. Res.*, *114*, B11102, doi:10.1029/2008JB006100.

Gregg, P. M., L. B. Hebert, L. G. J. Montési, and R. F. Katz (2012), Geodynamic models of melt generation and extraction at mid-ocean ridges, *Oceanography*, *25*, 8–88, doi:10.5670/oceanog.2012.05.

Grove, T. L., R. J. Kinzler, and W. B. Bryan (1992), Fractionation of mid-ocean ridge basalt (MORB), in *Mantle Flow and Melt Generation at Mid-Ocean Ridges, Geophys. Monogr. Ser., vol. 71*, edited by J. Phipps Morgan, D. K. Blackman, and J. M. Sinton, pp. 281–310, AGU, Washington, D. C.

Hebert, L. B., and L. G. J. Montési (2010), Generation of permeability barriers during melt extraction at mid-ocean ridges, *Geochem. Geophys. Geosyst.*, *11*, Q12008, doi:10.1029/2010GC003270.

Hebert, L. B., and L. G. J. Montési (2011), Melt extraction pathways at segmented oceanic ridges: Application to the East Pacific Rise at the Siqueiros transform, *Geophys. Res. Lett.*, *38*, L11306, doi:10.1029/2011GL047206.

Hékinian, R., D. Bideau, M. Cannat, J. Francheteau, and R. Hébert (1992), Volcanic activity and crust-mantle exposure in the ultrafast Garrett transform fault near 13°28′S in the Pacific, *Earth Planet. Sci. Lett.*, *108*, 259–275, doi:10.1016/0012-821X(92)90027-S.

Hékinian, R., D. Bideau, R. Hébert, and Y. Niu (1995), Magmatism in the Garrett transform fault (East Pacific Rise near 13°27′S), *J. Geophys. Res.*, *100*, 10,163–10,185, doi:10.1029/94JB02125.

Kaczmarek, M.-A., and O. Müntener (2008), Juxtaposition of melt impregnation and high-temperature shear zones in the upper mantle; Field and petrological constraints from the Lanzo Peridotite (Norther Italy), *J. Petrol.*, *49*, 2187–2220, doi:10.1093/petrology/egn065.

Kaczmarek, M.-A., and A. Tommasi (2011), Anatomy of an extensional shear zone in the mantle, Lanzo massif, Italy, *Geochem. Geophys. Geosyst.*, *12*, Q0AG06, doi:10.1029/2011GC003627.

Karson, J. A., M. A. Tivey, and J. R. Delaney (2002), Internal structure of uppermost oceanic crust along the Western Blanco Transform Scarp: Implications for subaxial accretion and deformation at the Juan de Fuca Ridge, *J. Geophys. Res.*, *107*(B9), 2181, doi:10.1029/2000JB000051.

Kastens, K. A., W. B. F. Ryan, and P. J. Fox (1986), Structural and volcanic expression of a fast slipping ridge-transform-ridge-plate boundary: Sea MARC I and photographic surveys at the Clipperton Transform Fault, *J. Geophys. Res.*, *91*, 3469–3488, doi:10.1029/JB091iB03p03469.

Katz, R. F. (2008), Magma dynamics with the enthalpy method: Benchmark solutions and magmatic focusing at mid-ocean ridges, *J. Petrol.*, *49*, 2099–2121, doi:10.1093/petrology/egn058.

Katz, R. F., and S. M. Weatherley (2012), Consequences of mantle heterogeneity for melt extraction at mid-ocean ridges, *Earth Planet. Sci. Lett.*, *335*, 226–237, doi:10.1016/j.epsl.2012.04.042.

Katz, R. F., M. Spiegelman, and C. H. Langmuir (2003), A new parameterization of hydrous mantle melting, *Geochem. Geophys. Geosyst.*, *4*(9), 1073, doi:10.1029/2002GC000433.

Kawasaki, I., Y. Kawahara, I. Takata, and N. Kosugi (1985), Mode of seismic moment release at transform faults, *Tectonophysics*, *118*, 313–327, doi:10.1016/0040-1951(85)90131-3.

Kelemen, P. B., and E. Aharonov (1998), Periodic formation of magma fractures and generation of layered gabbros in the lower crust beneath oceanic spreading ridges, in *Faulting and Magmatism at Mid-Ocean Ridges, Geophys. Monogr. Ser., vol. 106*, edited by W. R. Buck et al., pp. 267–289, AGU, Washington, D. C., doi:10.1029/GM106p0267.

Kelemen, P. B., and H. J. B. Dick (1995), Focused melt flow and localized deformation in the upper mantle: Juxtaposition of replacive dunite and ductile shear zones in the Josephine peridotite, SW Oregon, *J. Geophys. Res.*, *100*, 423–438, doi:10.1029/94JB02063.

Kelemen, P. B., H. J. B. Dick and J. E. Quick (1992), Formation of harzburgite by pervasive melt/rock reaction in the upper mantle, *Nature*, *358*, 635–641, doi:10.1038/358635a0.

Kelemen, P. B., G. Hirth, N. Shimizu, M. Spiegelman, and H. J. B. Dick (1997), A review of melt migration processes in the adiabatically upwelling mantle beneath oceanic spreading ridges, *Philos. Trans. R. Soc. London A*, *355*, 283–318, doi:10.1098/rsta.1997.0010.

Klein, F., R. Y. Koyanagi, J. S. Nakata, and W. R. Tanigawa (1987), The seismicity of Kilauea's magma system, in *Volcanism in Hawaii, U.S. Geol. Surv. Prof. Pap. 1350*, edited by R. W. Decker, T. L. Wright, and P. H. Stauffer, pp. 1019–1186. [Available at http://pubs.usgs.gov/pp/1987/1350/.]

Kodaira, S., T. Iidaka, A. Kato, J. O. Park, T. Iwasaki, and Y. Kaneda (2004), High pore fluid pressure may cause silent slip in the Nankai Trough, *Science*, *304*, 1295–1298, doi:10.1126/science.1096535.

Korenaga, J., and P. B. Kelemen (1997), Origin of gabbro sills in the Moho transition zone of the Oman ophiolite: Implications for magma transport in the oceanic lower crust, *J. Geophys. Res.*, *102*, 27,729–27,749, doi:10.1029/97JB02604.

Langmuir, C. H., and J. F. Bender (1984), The geochemistry of oceanic basalts in the vicinity of transform faults: Observations and implications, *Earth Planet. Sci. Lett.*, *69*, 107–127, doi:10.1016/0012-821X(84)90077-3.

© 2015. American Geophysical Union. All Rights Reserved.

Langmuir, C. H., J. F. Bender, and R. Batiza (1986), Petrological and tectonic segmentation of the East Pacific Rise, 5°30′–14°30′ N, *Nature*, *322*, 422–429, doi:10.1038/322422a0.

Langmuir, C. H., E. M. Klein, and T. Plank (1992), Petrological systematics of mid-ocean ridge basalts: Constraints on melt generation beneath ocean ridges, in *Mantle Flow and Melt Generation at Mid-Ocean Ridges, Geophys. Monogr. Ser., vol. 71*, edited by J. Phipps Morgan, D. K. Blackman, and J. M. Sinton, pp. 183–280, AGU, Washington, D. C.

Lawson, K., R. C. Searle, J. A. Pearce, P. Browning, and P. Kempton (1996), Detailed volcanic geology of the MARNOK area, Mid-Atlantic Ridge north of Kane transform, *Geol. Soc. London Spec. Publ.*, *118*, 61–102, doi:10.1144/GSL.SP.1996.118.01.05.

Lin, J., G. M. Purdy, H. Schouten, J. C. Sempere, and C. Zervas (1990), Evidence from gravity data for focused magmatic accretion along the Mid-Atlantic Ridge, *Nature*, *344*, 627–632, doi:10.1038/344627a0.

Liu, Y., J. J. McGuire, and M. D. Behn (2012), Frictional behavior of oceanic transform faults and its influence on earthquake characteristics, *J. Geophys. Res.*, *117*, B04315, doi:10.1029/2011JB009025.

Macdonald, K. C. (1982), Mid-ocean ridges: Fine scale tectonic, volcanic and hydrothermal processes within the plate boundary zone, *Annu. Rev. Earth Planet. Sci.*, *10*, 155–190, doi:10.1146/annurev.ea.10.050182.001103.

Macdonald, K. C., P. J. Fox, R. T. Alexander, R. Pockalny, and P. Gente (1996), Volcanic growth faults and the origin of Pacific abyssal hills, *Nature*, *380*, 125–129, doi:10.1038/380125a0.

Machado, N., J. N. Ludden, and C. Brooks (1982), Fine-scale isotopic heterogeneity in the sub-Atlantic mantle, *Nature*, *295*, 226–228, doi:10.1038/295226a0.

Magde, L. S., and D. W. Sparks (1997), Three-dimensional mantle upwelling, melt generation, and melt migration beneath segment slow spreading ridges, *J. Geophys. Res.*, *102*, 20,571–20,583, doi:10.1029/97JB01278.

McKenzie, D. P. (1985), ^{230}Th-^{238}U disequilibrium and the melting processes beneath ridge axes, *Earth Planet. Sci. Lett.*, *72*, 149–157, doi:10.1016/0012-821X(85)90001-9.

Menard, H. W., and T. Atwater (1969), Origin of fracture zone topography, *Nature*, *222*, 1037–1040, doi:10.1038/2221037a0.

Miller, M. M., T. Melbourne, D. J. Johnson, and W. Q. Sumner (2002), Periodic slow earthquakes from the Cascadia subduction zone, *Science*, *295*, 2423–2423, doi:10.1126/science.1071193.

Miller, K. J., W. L. Zhu, L. G. J. Montési, and G. A. Gaetani (2014), Experimental quantification of permeability of partially molten mantle rock, *Earth Planet. Sci. Lett.*, *388*, 273–282, doi:10.1016/j.epsl.2013.12.003.

Montési, L. G. J., and M. D. Behn (2007), Mantle flow and melting underneath oblique and ultraslow mid-ocean ridges, *Geophys. Res. Lett.*, *34*, L24307, doi:10.1029/2007GL031067.

Montési, L. G. J., M. D. Behn, L. B. Hebert, J. Lin, and J. L. Barry (2011), Controls on melt migration and extraction at the ultraslow Southwest Indian Ridge 10–16°E, *J. Geophys. Res.*, *116*, B10102, doi:10.1029/2011JB008259.

Murton, B. J., and I. G. Gass (1986), Western Limassol Forest complex, Cyprus: Part of an upper Cretaceous leaky transform fault, *Geology*, *14*, 255–258, doi:10.1130/0091-7613(1986)14<255:WLFCCP>2.0.CO;2.

Nicolas, A. (1986), A melt extraction model based on structural studies in mantle peridotites, *J. Petrol.*, *27*, 999–1022, doi:10.1093/petrology/27.4.999.

Nicolas, A. (1990), Melt extraction from mantle peridotites: Hydrofracturing and porous flow, with consequences for oceanic ridge activity, in *Magma Transport and Storage*, edited by M. P. Ryan, pp. 159–174, Wiley, N. Y.

Obara, K., H. Hirose, F. Yamamizu, and K. Kasahara (2004), Episodic slow slip events accompanied by non-volcanic tremors in southwest Japan subduction zone, *Geophys. Res. Lett.*, *31*, L23602, doi:10.1029/2004GL020848.

Pacheco, J. F., L. R. Sykes, and C. H. Scholz (1993), Nature of seismic coupling along simple plate boundaries of the subduction type, *J. Geophys. Res.*, *98*, 14,133–14,159, doi:10.1029/93JB00349.

Parmentier, E. M., and D. W. Forsyth (1985), Three-dimensional flow beneath a slow spreading ridge axis: A dynamic contribution to the deepening of the Median Valley toward fracture zones, *J. Geophys. Res.*, *90*, 678–684, doi:10.1029/JB090iB01p00678.

Perfit, M. R., et al. (1996), Recent volcanism in the Siqueiros transform fault: Picritic basalts and implications for MORB magma genesis, *Earth Planet. Sci. Lett.*, *141*, 91–108, doi:10.1016/0012-821X(96)00052-0.

Phipps Morgan, J., and Y. J. Chen (1993), The genesis of oceanic crust: Magma injection, hydrothermal circulation, and crustal flow, *J. Geophys. Res.*, *98*, 6283–6297, doi:10.1029/92JB02650.

Phipps Morgan, J., and D. W. Forsyth (1988), Three-dimensional flow and temperature perturbations due to a transform offset: Effects on oceanic crustal and upper mantle structure, *J. Geophys. Res.*, *93*, 2955–2966, doi:10.1029/JB093iB04p02955.

Phipps Morgan, J., E. M. Parmentier, and J. Lin (1987), Mechanisms for the origin of mid-ocean ridge axial topography: Implications for the thermal and mechanical structure of accreting plate boundaries, *J. Geophys. Res.*, *92*, 12,823–12,836, doi:10.1029/JB092iB12p12823.

Pockalny, R. A. (1997), Evidence of transpression along the Clipperton Transform: Implications for processes of plate boundary reorganization, *Earth Planet. Sci. Lett.*, *146*, 449–464, doi:10.1016/S0012-821X(96)00253-1.

Press, W. H., B. P. Flannery, S. A. Teukolsky, and W. T. Vetterling (2007), *Numerical Recipes: The Art of Scientific Computing*, 3rd ed., pp. 778–780, Cambridge Univ. Press, N. Y.

Reynolds, J. R., and C. H. Langmuir (1997), Petrological systematics of the Mid-Atlantic ridge south of Kane: Implications for ocean crust formation, *J. Geophys. Res.*, *102*, 14,915–14,946, doi:10.1029/97JB00391.

Roland, E., M. D. Behn, and G. Hirth (2010), Thermal-mechanical behavior of oceanic transform faults: Implications for the spatial distribution of seismicity, *Geochem. Geophys. Geosyst.*, *11*, Q07001, doi:10.1029/2010GC003034.

Rundquist, D. V., and P. O. Sobolev (2002), Seismicity of mid-oceanic ridges and its geodynamic implications: A review, *Earth Sci. Rev.*, *58*, 143–161, doi:10.1016/S0012-8252(01)00086-1.

Sandwell, D. T., and W. H. Smith (1997), Marine gravity anomaly from Geosat and ERS 1 satellite altimetry, *J. Geophys. Res.*, *102*, 10,039–10,054, doi:10.1029/96JB03223.

Schilling, J. G., R. H. Kingsley, and J. D. Devine (1982), Galápagos hot spot-spreading center system: 1. Spatial petrological and geochemical variations (83°W–101°W), *J. Geophys. Res.*, *87*, 5593–5610, doi:10.1029/JB087iB07p05593.

Schlindwein, V., A. Demuth, W. H. Geissler, and W. Jokat (2013), Seismic gap beneath Logachev Seamount: Indicator for melt focusing at an ultraslow mid-ocean ridge?, *Geophys. Res. Lett.*, *40*, 1703–1707, doi:10.1002/grl.50329.

Shen, Y., and D. W. Forsyth (1992), The effects of temperature- and pressure-dependent viscosity on three-dimensional passive flow of the mantle beneath a ridge-transform system, *J. Geophys. Res.*, *97*, 19,717–19,728, doi:10.1029/92JB01467.

Sinha, M. C., and R. L. Evans (2004), Geophysical constraints upon the thermal regime of the ocean crust, in *Mid-Ocean Ridges: Hydrothermal Interactions Between the Lithosphere and Oceans, Geophys. Monogr. Ser., vol. 148*, edited by C. R. German, J. Lin, and L. M. Parson, pp. 19–62, AGU, Washington D. C.

© 2015. American Geophysical Union. All Rights Reserved.

Smith, D. K., M. Tolstoy, C. G. Fox, D. R. Bohnenstiehl, H. Matsumoto, and M. J. Fowler (2002), Hydroacoustic monitoring of seismicity at the slow-spreading Mid-Atlantic ridge, *Geophys. Res. Lett.*, *29*(11), doi:10.1029/2001GL013912.

Smith, D. K., J. Escartin, M. Cannat, M. Tolstoy, C. G. Fox, D. R. Bohnenstiehl, and S. Bazin (2003), Spatial and temporal distribution of seismicity along the northern Mid-Atlantic ridge (15°–35° N), *J. Geophys. Res.*, *108*(B3), 2167, doi:10.1029/2002JB001964.

Sparks, D. W., and E. M. Parmentier (1991), Melt extraction from the mantle beneath spreading centers, *Earth Planet. Sci. Lett.*, *105*, 368–377, doi:10.1016/0012-821X(91)90178-K.

Spiegelman, M. (1993), Physics of melt extraction: Theory, implications and applications, *Philos. Trans. R. Soc. London A*, *342*, 23–41, doi:10.1098/rsta.1993.0002.

Standish, J. J., and K. W. W. Sims (2010), Young off-axis volcanism along the ultraslow-spreading Southwest Indian Ridge, *Nat. Geosci.*, *3*, 286–292, doi:10.1038/ngeo824.

Tepley, F. J., III, C. C. Lundstrom, K. W. W. Sims, and R. Hékinian (2004), U-series disequilibria in MORB from the Garrett Transform and implications for mantle melting, *Earth Planet. Sci. Lett.*, *223*, 79–97, doi:10.1016/j.epsl.2004.04.010.

The MELT Seismic Team (1998), Imaging the deep seismic structure beneath a mid-ocean ridge: The MELT experiment, *Science*, *280*, 1215–1218, doi:10.1126/science.280.5367.1215.

Thompson, G., and W. G. Melson (1972), The petrology of oceanic crust across fracture zones in the Atlantic Ocean: Evidence of a new kind of sea-floor spreading, *J. Geol.*, *80*, 526–538.

Thompson, G., W. B. Bryan, R. Ballard, K. Hamuro, and W. G. Melson (1985), Axial processes along a segment of the East Pacific Rise. 10°-12°N, *Nature*, *318*, 429–433, doi:10.1038/318429a0.

van Keken, P. E., et al. (2008), A community benchmark for subduction zone modeling, *Phys. Earth Planet. Inter.*, *171*, 187–197, doi:10.1016/j.pepi.2008.04.015.

Vidale, J. E., and P. M. Shearer (2006), A survey of 71 earthquake bursts across southern California: Exploring the role of pore fluid pressure fluctuations and aseismic slip as drivers, *J. Geophys. Res.*, *111*, B05312, doi:10.1029/2005JB004034.

Wang, T., J. Lin, B. Tucholke, and Y. J. Chen (2011), Crustal thickness anomalies in the North Atlantic Ocean basin from gravity analysis, *Geochem. Geophys. Geosyst.*, *12*, Q0AE02, doi:10.1029/2010GC003402.

Weatherley, S. M., and R. F. Katz (2010), Plate-driven mantle dynamics and global patterns of mid-ocean ridge bathymetry, *Geochem. Geophys. Geosyst.*, *11*, Q10003, doi:10.1029/2010GC003192.

Wendt, J. I., M. Regelous, Y. Niu, R. Hékinian, and K. D. Collerson (1999), Geochemistry of lavas from the Garrett Transform Fault: Insights into mantle heterogeneity beneath the eastern Pacific, *Earth Planet. Sci. Lett.*, *173*, 271–284, doi:10.1016/S0012-821X(99)00236-8.

Wesson, R. L. (1988), Dynamics of fault creep, *J. Geophys. Res.*, *93*, 8929–8951, doi:10.1029/JB093iB08p08929.

Wilcock, W. S., G. M. Purdy, and S. C. Solomon (1990), Microearthquake evidence for extension across the Kane transform fault, *J. Geophys. Res.*, *95*, 15,439–15,462, doi:10.1029/JB095iB10p15439.

White, R. S., D. McKenzie, and R. K. O'Nions (1992), Oceanic crustal thickness from seismic measurements and rare earth element inversions, *J. Geophys. Res.*, *97*, 19,683–19,715, doi:10.1029/92JB01749.

Zhu, W., and G. Hirth (2003), A network model for permeability in partially molten rocks, *Earth Planet. Sci. Lett.*, *212*, 407–416, doi:10.1016/S0012-821X(03)00264-4.

Zhu, W., G. A. Gaetani, F. Fusseis, L. G. J. Montési, and F. De Carlo (2011), Microtomography of partially molten rocks: Three-dimensional melt distribution in mantle peridotite, *Science*, *332*, 88–91, doi:10.1126/science.1202221.

© 2015. American Geophysical Union. All Rights Reserved.